Effect of Wet and Dry Conditions on Wear Behavior of Amorphous Coating of Fe-Cr-Mo-Nb-C-B

F. Farzan , H. R. Shahverdi* and F. Malek Ghaeni

* *shahverdi@modares.ac.ir*

Received: November 2017 Accepted: March 2018

Department of Materials Science and Engineering, Tarbiat Modares University, Tehran, Iran.

DOI: 10.22068/ijmse.15.2.76

Abstract: *Recently, wear resistant properties of metallic glasses has attracted a lot of interest. Because the surface of metallic glasses are prone to phase transformation, finding the effects of test condition on structure and wear behavior of metallic glasses is important. In this research, by using an automated electrospark deposition (ESD), a layer of $Fe_{51}Cr_{18}Mo_7B_{16}C_4Nb_4$ was deposited on AISI 316l stainless steel. Metallographic, scanning electron microscope (SEM) and Energy-dispersive X-ray spectroscopy (EDS) analyses of the coating were conducted for measuring the thickness and analyzing composition of the coating. X-ray diffraction (XRD), Transmission electron microscopy (TEM) and selected area electron diffraction (SAED) investigations showed that the structure of the coating was amorphous. Ball on disc wear tests were conducted in dry and wet conditions and Ringer's solution was chosen as the wetting agent. The wear test results showed that the coefficient of friction in dry condition was lower than the wet condition and wear modes were fatigue and corrosive wear in dry and wet conditions respectively. SEM and EDS analyses showed different features and elemental inhomogeneity on the surface of the dry wear track, which were not detectable in wet wear track. In addition, activation of diffusion process and formation of carbides and borides were observed on the wear track in dry condition.*

Keywords: *Fe-based, Amorphous coating, Electrospark deposition (ESD), Wear behavior.*

1. INTRODUCTION

Among coating processes that could deposit 10-100 µm thick layers, electrospark deposition (ESD) as an arc welding process has the advantages of high cooling rate (105-106 K/s) and low heat input [1]. These characteristics enable ESD to reduce heat affected zone (HAZ) and keep the microstructure of the substrate unchanged. Ebrahimnia et al. showed that the low heat input has a predominant effect on buildup of the coating [2]. On the other hand, ESD is an environmentally friendly process and does not produce any hazardous waste. Nowadays some of the ESD applications include repairing fine cracks of dies and flanges and depositing hard coatings on small pieces such as surgical instruments [3]. ESD process has been used to deposit a wide variety of industrial alloys such as iron based alloys [4], titanium based alloys [5], cobalt based alloys [6], nickel based alloys [7] and aluminum based alloys [8]. Moreover, amorphous-nanocrystalline [9] and composite [10] coatings could be achieved by using the process because of its fine control on depositing parameters. Therefore, according to the ESD advantages and its low operation cost, it could find more applications for depositing amorphous coatings.

Among different alloys that have been used to synthesize bulk metallic glasses (BMGs), Fe-based alloys are categorized as late transition metal (LTM)-BMGs. These alloys were developed due to material costs and the availability of raw material deposits [11]. LTMs are more suitable for industrial applications and various Fe, Co and Ni based metallic glasses have been proposed for wear resistant applications[12]. Among Fe-based alloys that have been proposed for synthesizing amorphous phases, Fe-Cr-Nb-B, Fe-Cr-Mo-C and Fe-Cr-Mo-B systems have been proposed by Koga [13], Inoue [14] and Prakash [15] for wear resistant applications. Ahmadi et al. [16] showed that Niobium in $Fe_{51}Cr_{18}Mo_7B_{16}C_4Nb_4$ (at%) alloy slows down the diffusion processes and increase the crystallization temperature which lead to increasing glass forming ability (GFA). Zohdi et al. [15, 16] showed that amorphous ribbons of $Fe_{51}Cr_{18}Mo_7B_{16}C_4Nb_4$ had higher corrosion resistance than that of 316L stainless steel and Ti–6Al–4V and Fakoori et al. [19] have reported

production of amorphous coating of $Fe_{48}Cr_{18}Mo_7B_{16}C_4Nb_7$. Therefore, production of $Fe_{51}Cr_{18}Mo_7B_{16}C_4Nb_4$ alloy because of advantages such as high GFA, high corrosion resistance and high hardness has the potential of industrial uses as an amorphous coating.

Deposition of Fe-based precursors by ESD has the advantage of high hardness (up to 17 GPa) which is suitable for wear resistant applications [20]. On the other hand, amorphous structure is not thermodynamically a stable phase and environmental parameters can trigger phase transformation in amorphous coating. For this reason, finding the effects of operating condition on the microstructure of the amorphous structures is necessary for explaining macroscopic behaviors. The goal of this research is to investigate the probability of phase transformation during wear process of an amorphous coating of $Fe_{51}Cr_{18}Mo_7B_{16}C_4Nb_4$. After depositing and characterizing the coating, wear behavior of the coating was studied in two different conditions. Then the effects of the test conditions on the microstructure and macroscopic behavior of the coating were investigated.

2. MATERIALS AND METHODS

2. 1. Materials

$Fe_{51}Cr_{18}Mo_7B_{16}C_4Nb_4$ (%at) ingot was melted by vacuum induction melting furnace from industrial raw materials. The raw materials were ferro-niobium (>65%wt Nb), ferro-molybdenum (>60%wt Mo), ferro-chromium (>65%wt Cr), iron (>99%wt Fe), ferro-boron (>17%wt B) and graphite (>99%wt C). The ingot was cut into 3mm diameter and 60 mm length rods by CNC wire-cut EDM as ESD electrode. The substrate was 1mm thick sheet of AISI 316l stainless steel that was cut into 2×2 cm^2 squares. Chemical compositions of the electrode and the substrate are shown in Table 1.

1. 2. Coating Procedure

For eliminating the dependence of coating quality on user's skill, coatings were deposited by an automated-ESD. The instrument was homemade and the current source was RC pulse generator. The voltage was 15V and the current was controlled by changing the resistance of the circuit. The capacitance and resistance ranges of the instrument were from 10-2000 μf and 1-70 Ω respectively. The mechanical parts of the instrument are shown schematically in Fig. 1. The applicator was able to move in z direction and the sample was displaced in x and y directions by stepper motors. The normal load of the electrode to substrate was controlled by a lever and a weight on the other side of the applicator was hanged by an elastic rope for damping mechanical vibrations. By changing the amount and position of the weight, it was possible to control the normal force of the electrode with a precision of ±0.05N. There was ~1cm gap between the samples and x,y-table for air cooling in the sample holder. The angle between applicator and lever was adjustable by the applicator holder. Angle between the electrode axis and the line normal to the substrate was measured as diagonal angle.

All the selected parameters for coating $Fe_{51}Cr_{18}Mo_7B_{16}C_4Nb_4$ on the substrate is given in table 2. Before coating process, substrates were ground with silicon carbide paper No. 400 and were cleaned by propanol. The depositing process was repeated 8 times for the same scanning area.

1. 3. Characterization Procedure

For preparing cross-sections of the samples, samples were cut with saw and were mounted. Then the samples were grounded with silicon carbide papers No. 120, 240, 400, 600, 800, 1200 and 2000 grit in series. Then the samples were

Table 1. Chemical composition of electrode and substrate in weight and atomic percent

Element	B	C	Cr	Fe	Mn	Mo	Nb	Ni	Si
Electrode (wt %)	3.4	1	18.5	56.4	-	13.3	7.4	-	-
Substrate (wt %)	-	0.03	18	62	2	3	-	14	0.75

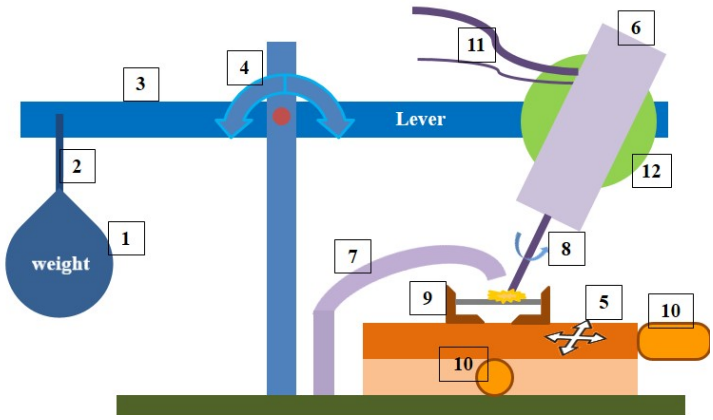

Fig. 1. schematic image of mechanical parts of the automated-ESD: (1) balance weight, (2) elastic rope, (3)lever, (4) fulcrum, (5) x,y table, (6) applicator, (7)Argon tube, (8) electrode, (9)sample holder, (10) stepper motor, (11)cable connectors of motor and electrode, (12) applicator holder.

Table 2. The selected parameters for depositing of $Fe_{51}Cr_{18}Mo_7B_{16}C_4Nb_4$ coatings

Parameter	Level
X scanning speed	1.5mm/s
Y scanning step	1.3mm/line
Normal force	1±0.1N
Capacitance	20µf
Electrode Rotational speed	3500 ± 500 rpm
Diagonal angle	30° ± 5°
Number of passes	8
Current	4 ± 1 A
Argon flow	~2 lit/min

polished by alumina powder (< 0.3 µm) and were etched by Glyceregia solution (15 cc HCl +10 cc Glycerol + 5 cc HNO_3). Optical metallographic investigations were conducted by an Olympus BX51M apparatus. SEM analysis was carried out in a MIRA3 TESCAN operating at 15 kV after gold sputtering on the samples. Surface roughness measurement was conducted by using a Taylor-Hobson model Surtronic 25 profilometer with an accuracy of 2 % on a 4 mm segment of the coating.

X-ray diffraction (XRD) and transmission electron microscopy (TEM) analyses were conducted for microstructural investigations of the coating. XRD analysis was carried out by an X'Pert MPD Philips apparatus equipped with an X-ray Co tube (Co $K_{\alpha 1}$, λ=1.78897 Å). XRD patterns were collected over a 2θ range from 20° to 100° with a step size of 0.04° and a counting time of 0.8 s per step. TEM sample was prepared by separating the coating from the substrate. After bending the substrate for several times, the detached particles from the substrate were collected by a brush. Fine particles were ultrasonically dispersed in ethanol and one droplet was dropped on to a carbon coated copper grid and dried in ambient condition. TEM instrument was Philips CM30 and the images were formed at an accelerating voltage of 150 kV.

Wear tests were conducted by a ball-on-disc instrument that was developed in Tarbiat Modares University. Balls of AISI 52100 steel (5mm diameter) were chosen as the counterpart. Wear tests were performed under a normal load of 10 N, tangential speed of 0.2 m/s and 600 m sliding distance. Ringer's solution was chosen as the wetting agent which its composition is given in Table 3, according to its data sheet. All the wear tests were conducted 3 times for wet and dry samples in ambient condition.

Table 3. Composition of ingredients in 100 ml Ringer's solution.

Ingredient	Composition (g)
NaCl	0.86
KCl	0.03
$CaCl_2.2H2O$	0.033

2. RESULTS AND DISCUSSION

2. 1. Microstructural Investigation

An optical top view image of a 2×6 cm^2 sample is given in Fig. (2-a) that indicates the automation set-up was able to deposit the coating in centimeter scale. Profilometry of the coating showed that arithmetic average roughness (Ra) = 3.63 µm, maximum peak height (R_p) = 10 µm and maximum valley depth (R_v) = 11 µm. Optical microscopy of cross sectional view of the coating is given in Figs. (2-b) and (2-c) at magnifications of 200X and 500X respectively. According to these figures, there was no void or separation between depositing passes in the coating and the interface; moreover, the coating thickness was ~30-50µm. Fig. (2-d) and (2-e) show SEM images of top view of the coating at 1000X and 5000X. According to Fig. (2-d), the droplets that were separated from the electrode have completely covered the surface. Fig. (2-e) shows some cracks through droplets during solidification. Because solidification rate of the

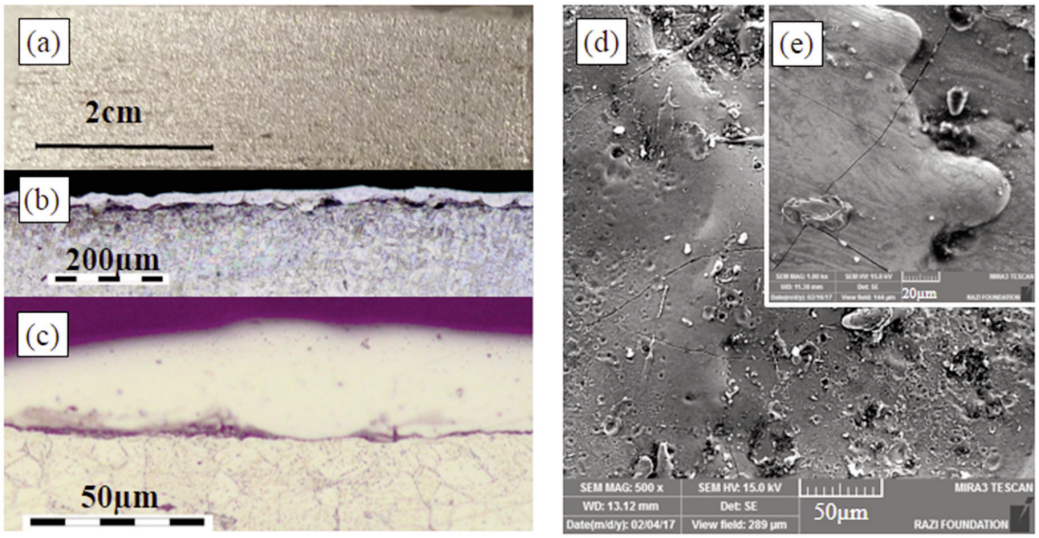

Fig. 2. Optical image of the coating (a), metallographic images of deposited coating at 200X (b) and at 500X (c), SEM image of the top view of the coating at 1000X (d), and 5000X (e).

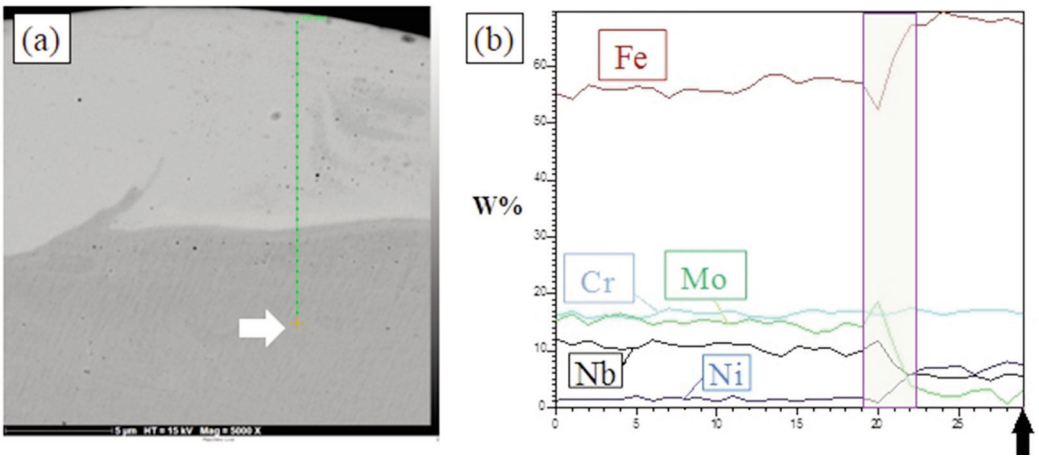

Fig. 3. BSE image (a) and EDS analyses (b) across the coating and the substrate; corresponding points are displayed by bold arrows.

molten droplets was fast and shrinkage was inevitable, these cracks are unavoidable and generally were appeared inside the droplets. Though these cracks confined to the last depositing pass, they were not deep and the following depositing passes could cover them. Therefore, as it is seen in Fig. (2-c) these cracks do not propagate through coating thickness.

Back-scattered electrons (BSE) image and Energy-dispersive X-ray spectroscopy (EDS) analyses across the coating and the substrate are given in Figs. (3-a) and (3-b) respectively. The transition zone, which is marked by a rectangle in Fig. (3-b), is not very broad and indicates that the composition of the upper part of the coating is similar to the electrode composition. For quantifying the probability of electrode and substrate mixing during deposition, Palatnik criterion could be used [21]. This criterion is a ratio based on physical properties of anode and cathode that is given in equation (1).

$$\frac{\tau_a}{\tau_c} \cong \frac{C_a d_a \lambda_a (T_a - T_0)^2}{C_c d_c \lambda_c (T_c - T_0)^2} \quad (1)$$

where τ_a, τ_c are the characteristic times for formation of melting and evaporation spots on the surface of anode and cathode; C_a, C_c, d_a, d_c, λ_a, λ_c, T_a, T_c are the heat capacities, densities, thermal conductivities and melting points of anode and cathode respectively, and T_0 is ambient temperature. According to this criterion if τ_a/τ_c ~1; intense vaporization on both poles occurs simultaneously [22]. Since migration and solidification of electrode droplets to substrate is fast, there is no time for solving substrate elements in liquid state; therefore mixing of electrode and substrate alloys occurs in vapor state and the importance of finding intense vaporization zones is helpful for predicting the composition and size of the transition zone. In this research, both electrode and substrate were Fe-based alloys with similar amount of chromium, and they had similar elements such as molybdenum in their compositions, therefore physical properties of the anode and cathode could be somewhat near each other. In this case, Palatnik criterion for this condition could approximate to 1 and consequently mixing electrode and substrate was expected in the early passes. However, because evaporation was on both poles, after several passes, the concentration of substrate elements was reduced and the composition of later passes became more similar to the electrode composition. In addition, EDS analysis in Fig. (3-b) shows this compositional trend and the concentrations of iron, chromium and molybdenum are in consonance with Table 1 data. Nevertheless, niobium concentration in coating and substrate are ~5% higher than the data in Table 1; which might be because of Nb Lα (2.166 keV) and Au Mα (2.120 keV) are near each other [23].

For characterization of coating crystallinity, XRD, TEM and SAED analyses were conducted. XRD analysis of the coating is given in Fig. (4-a); the broad peak from 2θ=40 to 2θ=60 indicates the presence of the amorphous structure in the coating. XRD analysis of the substrate is given in

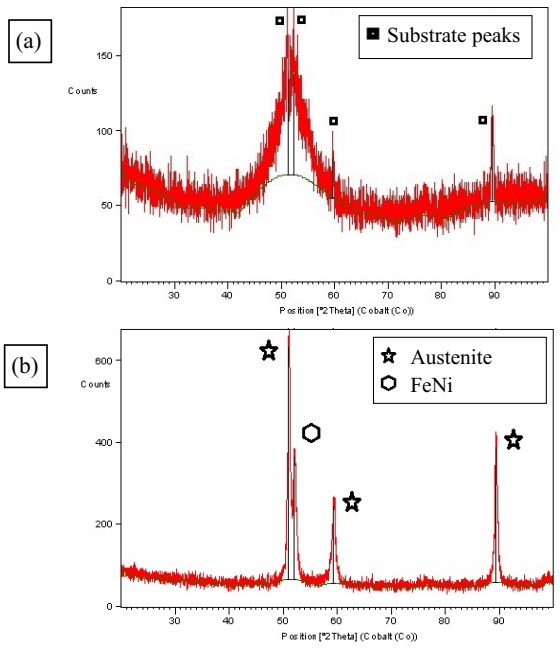

Fig. 4. XRD analysis of the coating (a) shows a broad peak that indicates on the presence of amorphous phase and XRD analysis of the substrate (b) shows that the distinct peaks in the coating analysis relates to the substrate. Austenite peaks ( ) according to refrence code of 00-023-0298 and FeNi peaks ( ) according to reference code of 00-003-1044.

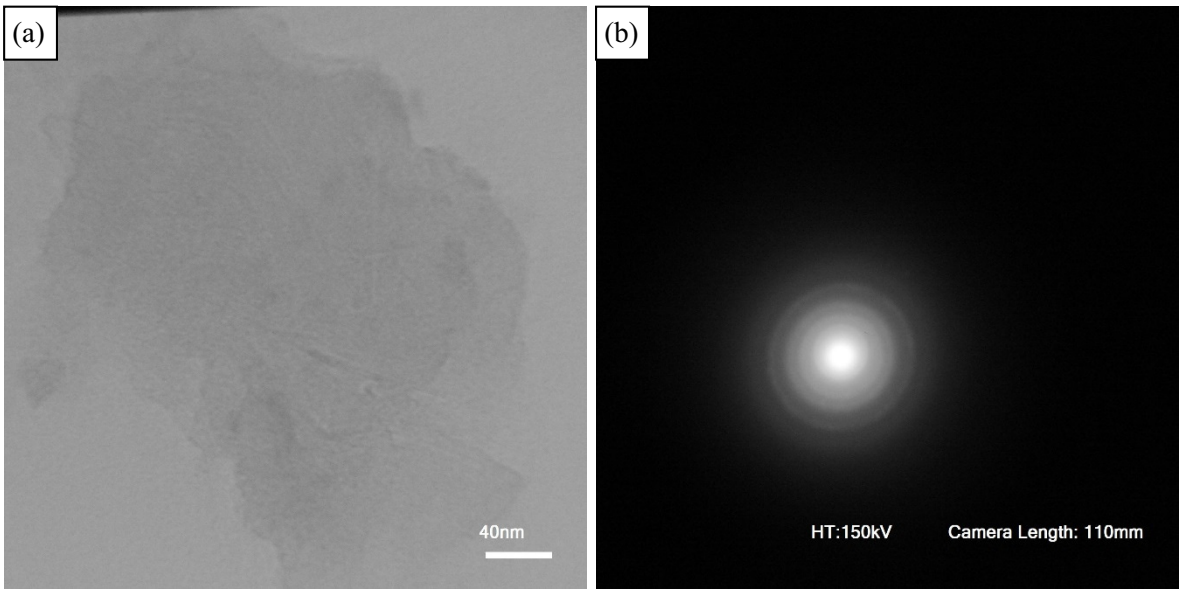

Fig. 5. Bright field TEM image (a) and SAED pattern (b) of the coating indicate that the structure of the coating is amorphous.

Fig. (4-b). It shows four peaks that are related to austenite and FeNi phases in 316l stainless steel. On the other hand, these four peaks have the same position in the XRD analysis of the coating. Therefore, there is no distinct peak in Fig. (4-a) that relates to the coating structure and it indicates that the structure of the coating is amorphous. Fig. (5-a) shows bright field image of the coating and Fig. (5-b) shows SAED pattern of the coating. There is no distinct pattern in SAED and the halo indicates the amorphous structure of the coating.

2. 2. Wear Behavior Investigation

Ball on disc wear test results are given in Fig. 6. As it is shown, unusually friction coefficient in dry condition was lower than the wet condition. The results indicated happening of a phenomenon during the wear test that could change the wear mechanism and its effect was more effective than the lubricating effect of the wetting agent in reducing friction coefficient. Among parameters that have effects on friction coefficient, morphological parameters could not be involved in this case; because all the samples were similar to each other and the coatings were deposited automatically by the same parameters. One of the main parameters that could affect wear rate and wear mode is hardness ratio of abraded material to abrasive material [24]. In most metallic glasses, surface crystallization has been observed to occur even at temperatures far below any crystallization event in the bulk. Preferred nucleation and/or accelerated growth may occur at the surface because of a decrease in the total surface energy, the greater ease of diffusion and stress relaxation, or a local change in the surface composition. Local changes in surface composition by selective oxidation or segregation are assumed to possess the strongest influence on surface crystallization [25]. In wear process, time scales are very short and all the energy of frictional work dissipates through small contacts which leads to high but transient local temperatures [26]. Therefore, surface of amorphous coatings are prone to phase transformations and temperature fluctuations during wear process in dry condition could induce phase transformation and change surface microstructure. On the other hand, wet condition suppresses temperature fluctuation and consequently prevents phase transformation.

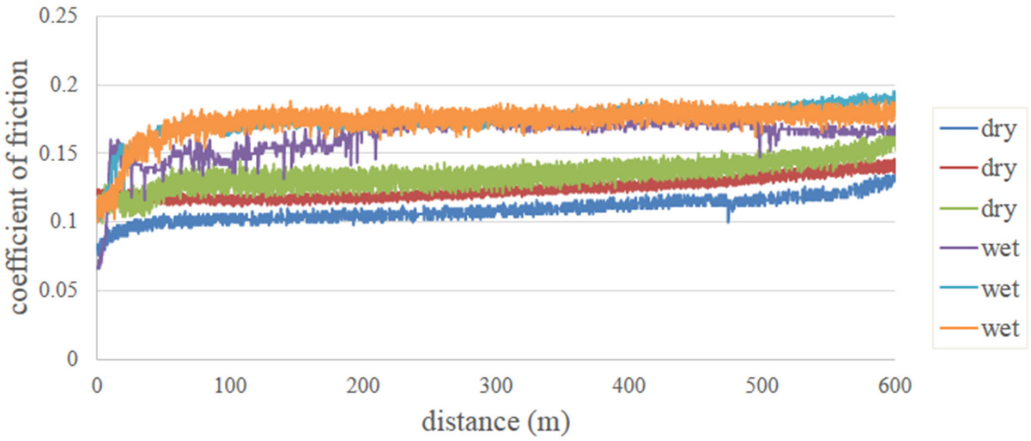

Fig. 6. Ball on disc wear test for coatings in dry and wet conditions.

Thermodynamic and kinetic investigations into phase transformations of Fe-Cr-Mo-C-B and Fe-Cr-Mo-Nb-C-B alloys have been conducted by other researchers. Ahmadi et al. [24, 25] have reported formation of ferrite and chi nano-crystals in amorphous ribbons of Fe-Cr-Mo-Nb-C-B at temperatures lower than 600°C. Saremi [29] showed that annealing the amorphous ribbons of Fe-Cr-Mo-Nb-C-B at temperatures higher than 700°C led to the precipitation of borides and carbides and the increasing hardness to ~15GPa (~1500HV). Duarte et al. [30] showed that after heating amorphous ribbons of Fe-Cr-Mo-C-B up to 440°C in a ramp of 20 K/s and subsequent cooling down to room temperature, crystallites with an average size of 21±5 nm embedded in the amorphous matrix of $Fe_{50}Cr_{15}Mo_{14}C_{15}B_6$ were observed. They showed that heating the samples led to nucleation of α-Fe, χ-$Cr_6Fe_{18}Mo_5$, $M_{23}(C,B)_6$, M_7C_3, M_6C (η-Fe_3Mo_3C) and $FeMo_2B_2$, with M=Fe, Cr, Mo sequentially in less than 2 minute. Also at temperatures higher than 777°C, the final equilibrium structure was reached, which was composed of 71.7% $M_{23}(C,B)_6$, 23.1% η-Fe_3Mo_3C and 5.2% $FeMo_2B_2$ phases. Moreover, adding Nb to Fe-Cr-Mo-C-B systems increased probability of M_6C carbides formation [31]. Duarte et al. [32] showed that formation of these precipitates change concentration of elements about 30% in 5nm distance at the interface of precipitates. Therefore, formation of carbides and borides are thermodynamically favorable in amorphous system of Fe-Cr-Mo-Nb-C-B and it might lead to structural changes in the coating.

Figs. (7-a) and (7-d) show top view of wear tracks in dry and wet conditions at magnification of 1000X. As it is seen, just asperities peaks were eroded which are labeled as wear zone. Therefore, the real contact area of ball and coating was confined to small area of the asperities peaks. Reduction of contact area increases localized heat transfer, which amplifies localized temperature fluctuations. Temperature fluctuation is one of the basic requirements that increase the possibility of phase transformation during wear test. Figs. (7-b) and (7-e) show top view of wear zone in dry and wet conditions at magnification of 20,000X. Fig. (7-b) shows cracks and spalling on the wear zone of dry sample but according to Fig. (7-e), there is no considerable feature on the wear zone of wet sample. Figs. (7-c) and (7-f) show BSE images of wear zones at magnification of 10,000X of dry and wet samples. Fig. (7-c) shows some features that might be the consequence of formation of phases that are harder than the matrix or their conductivity are lower than the matrix in dry sample. Nevertheless, Fig. (7-f) shows no observable feature on the wet sample. Surface changes in dry sample, which are not detectable in wet sample, could be related to higher probability of phase transformation in dry condition. Because in wet condition cooling effect of water can suppress temperature fluctuation and increase heat dissipation. On the

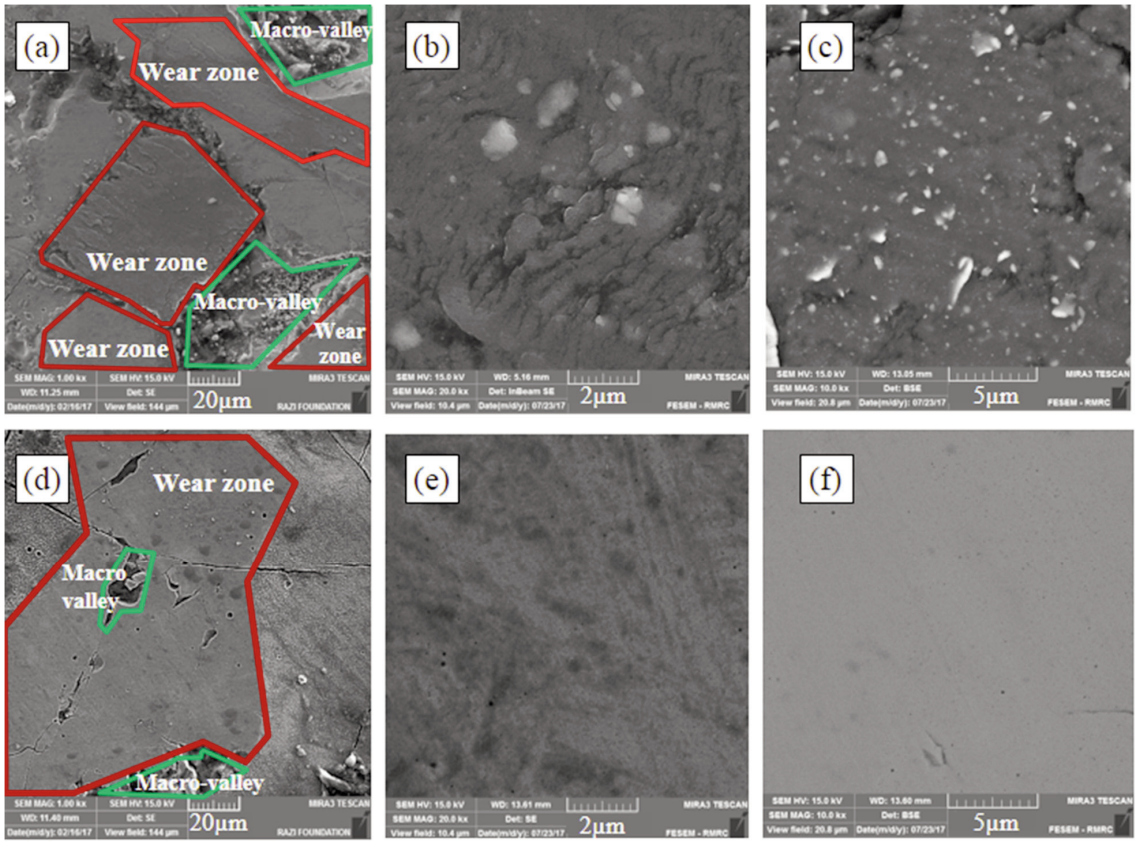

Fig. 7. SEM images of the wear tracks in dry (a, b and c) and wet (d, e and f) conditions. SE images at 1000X (a and d) from top view of wear track; SE images at 20,000X (b and e) and BSE images at 10,000X (c and f) from wear zones.

other hand, in dry condition not only temperature fluctuation was higher but also because of weak heat dissipation, the temperature of the sample could increase.

One of the important parameters that affect coefficient of friction is wear mode. Elemental analysis of the wear track is given in Fig. 8. According to Fig. (8-a); Cr, Mo and Nb depletion and oxide formation were observed in wear track of dry sample. On the other hand, according to Fig. (8-b), oxide formation happened on both wear track and unworn part of the coating in the wet sample and no elemental depletion was observed on the wet wear track. Spalling and cracks that are not tangential to the surface are characteristics of fatigue wear and flat surface and oxide formation are characteristics of corrosive wear [33]. Therefore, according to Figs. (7-b) and (8-a) the mode of wear in dry condition was fatigue wear and according to Figs. (7-e) and (8-b) the mode of wear in wet condition was corrosive wear. In fatigue wear, adhesiveness or abrasiveness are not necessary for generation of wear particles. On the other hand, in corrosive wear, sliding should remove tribochemical reaction products [24]. Therefore, these different wear modes might be the reason of difference of friction coefficients that were shown in Fig. 6.

Fig. 9 shows morphology and elemental analysis of the features that are given in Fig. (7-c) of dry sample at magnification of 50,000X. Fig. (9-a) shows spalling on the wear zone of the coating in the immediate vicinity of a bright spot. Morphology and elemental analyses of one of these bright spots are given in Figs. (9-b) and (9-c), respectively. Fig. (9-b) shows crack formation around the large bright spot and formation of several small bright spots all over the surface. Fig. (9-c) shows line scan analysis of the bright spot in Fig. (9-b). As it is shown, the content of B, C, Nb, Cr and Mo increases in the bright spots. According to the thermodynamic and kinetic

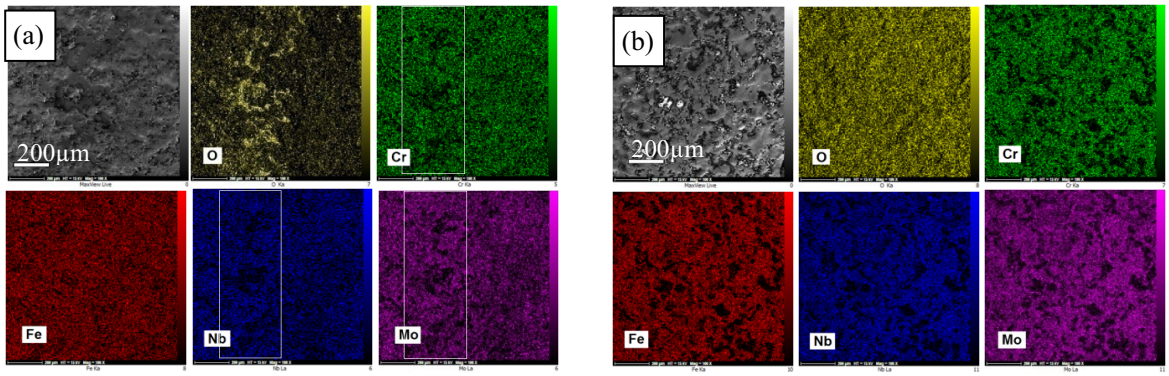

Fig. 8. Elemental map analyses of wear track in dry condition (a) and wet condition (b). In dry condition, the oxide phase is formed on wear track but in wet condition, the oxide phase is formed all over the coating. Moreover, chromium, niobium and molybdenum depletion is detected in dry wear track; but in wet wear test, there is uniformity between wear track and the other parts of the coating.

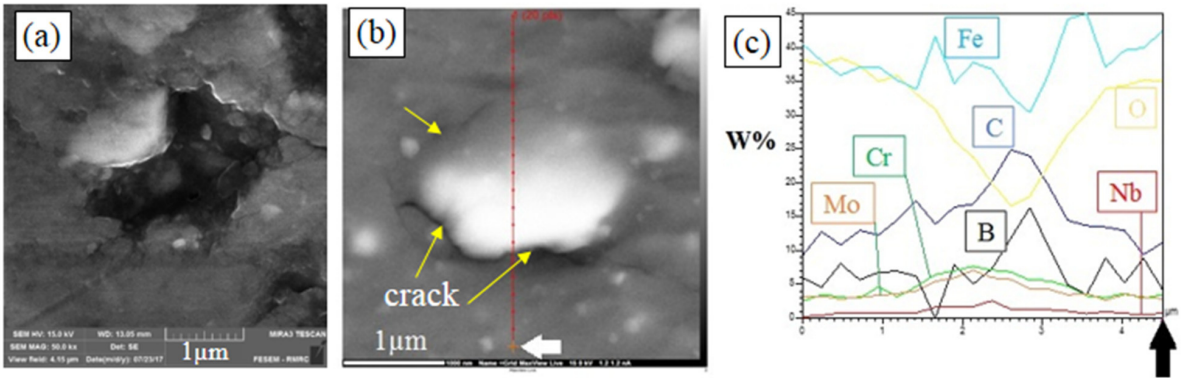

Fig. 9. (a) Formation of precipitates and voids near each other on the wear zone in dry condition test; (b) formation of cracks near precipitates in dry condition test; (c) EDS analysis of precipitates shows higher amount of C and B in precipitates and also an increase in Cr, Mo and Nb content. corresponding points in (b) and (c) are displayed by bold arrows.

investigations of Fe-Cr-Mo-Nb-B-C systems, these bright spots are carbides or borides of chromium or molybdenum or niobium or a mixture of them. These phases generally are harder than the matrix and have lower electrical conductivity than metallic matrix. Formation of these hard phases because of temperature fluctuation and activation of diffusion processes was the reason of increasing hardness and changing the wear mode. Another effect of formation of carbides and borides was nucleation of cracks because of atomic migration and structural changes. These inhomogenities and cracks could increase local stresses which might exceeds yield stress and reduce fatigue life [24]. This process might lead to detachment of some parts of the coating, which is shown in Fig. (9-a). In addition, these particles are rich in Cr, Mo and Nb and detachment of them make depletion of these elements on the surface which is shown in Fig. (8-a).

Probable steps during dry wear test are schematically presented in Fig. 10. Ball rotation on asperities of the coating heated the peaks (Fig. (10-a)). Because the kinetics of phase transformation in amorphous structures were in second and minute time scales and the test lasted for 50 minutes, thermodynamically stable phases such as chi, carbides and borides could precipitate which were rich of Cr, Mo and Nb. Elemental diffusion during phase transformation were able to make structural miss-match between

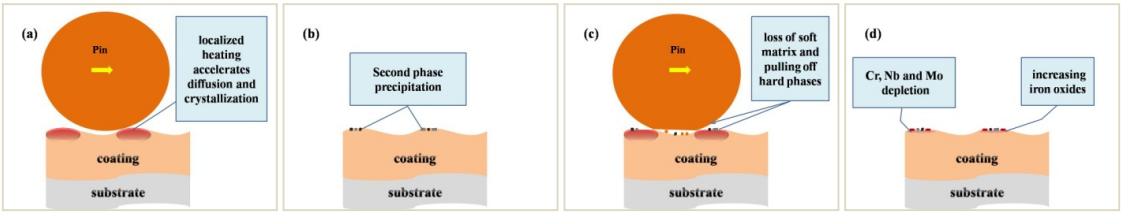

Fig. 10. Proposed wear mechanism for $Fe_{51}Cr_{18}Mo_7B_{16}C_4Nb_4$ amorphous coating in dry condition.

the precipitates and matrix (Fig. (10-b)). Then rotation of the ball repeatedly propagated micro-cracks and separated precipitates (Fig. (10-c)). Finally, protective layer was destroyed and iron oxides formed (Fig. (10-d)).

CONCLUSIONS

Optical microscope and SEM investigations showed that automation of ESD was useful for eliminating coating quality dependency on user's skill. EDS analysis revealed that the transition zone between substrate (316l stainless steel) and the coating ($Fe_{51}Cr_{18}Mo_7B_{16}C_4Nb_4$) was confined to the early deposition passes and the composition of the upper part of the coating was similar to the electrode composition. Moreover, TEM and XRD analyses of the coating indicated the structure of the coating was amorphous.

Ball on disc wear test of the coating showed lower coefficient of friction in dry condition than the wet condition. Analyses of the wear tracks showed fatigue and corrosive wear modes in dry and wet conditions respectively. BSE imaging and EDS analysis of the wear zones indicated activation of diffusion process in dry condition wear test and no precipitation was observed in wet condition. Based on the observations, parameters such as temperature fluctuations and amorphous structure of the coating made precipitation of secondary phases such as carbides or borides possible in dry condition wear test. On the other hand, cooling effect of water suppressed temperature fluctuation and consequently diffusion process did not occur in wet condition.

ACKNOWLEDGMENT

This research is supported by Tarbiat Modares University, Iran.

REFERENCES

1. Cadney, S. and Brochu, M., Formation of Amorphous Zr_{41}.2Ti13.8Ni10Cu12.5Be22.5 Coatings Via the Electrospark Deposition Process. Intermetallics, 2008, 16, 518–523.
2. Ebrahimnia, M., Ghaini, F. M., Xie, Y. J. and Shahverdia, H., Microstructural Characteristics of the Built Up Layer of a Precipitation Hardened Nickel Based Superalloy By Electrospark Deposition-ESD. Surf. Coatings Technol., 2014, 258, 515–523.
3. "Electrospark Deposition for Depot- and Field-Level Component Repair and Replacement of Hard Chromium Plating", Sartwell, B. D., Legg, K. O., Price, N., Aylor, D., Champagne, V., Pepi, M., Pollard, T., http://www.dtic.mil/docs/citations/ADA603502
4. Liu, D., Gao, W., Li, Z., Zhang, H. and Hu, Z., Electro-Spark Deposition of Fe-Based Amorphous Alloy Coatings. Mater. Lett., 2007, 61, 165–167.
5. Durdu, S., Aktug, S. L. and Korkmaz, K., Characterization and Mechanical Properties of the Duplex Coatings Produced on Steel by Electro-Spark Deposition and Micro-Arc Oxidation. Surf. Coatings Technol., 2013, 236, 303–308.
6. Depczyński, W. and Radek, R., "Properties of electro spark deposited stellite coating on mild steel". Proceedings of the 22nd Int. Conf. on Metallurgy and Materials (METAL), Brno, Czech Republic, 2013, 15-21.

7. Ebrahimnia, M., Ghaini, F. M. and Shahverdi, H. R., Hot Cracking in Pulsed Laser Processing of a Nickel Based Superalloy Built Up by Electrospark Deposition. Sci. Technol. Weld. Join., 2014, 19, 25–29.
8. Milligan, J., Heard, D. W. and Brochu, M., Formation of Nanostructured Weldments in the Al – Si System Using Electrospark Welding. Appl. Surf. Sci., 2010, 256, 4009–4016.
9. Hong, X., Tan, Y., Zhou, C., Xu, T. and Zhang, Z., Microstructure and Tribological Properties of Zr-based Amorphous-Nanocrystalline Coatings Deposited on the Surface of Titanium Alloys by Electrospark Deposition. Appl. Surf. Sci., 2015, 356, 1244–1251.
10. Wang, R. J., Qian, Y. Y. and Liu, J., Structural and Interfacial Analysis of WC92-Co8 Coating Deposited on Titanium Alloy by Electrospark Deposition. Appl. Surf. Sci., 2004, 228, 405–409.
11. Inoue, A., Shen, B. and Nishiyama, N., Development and Applications of Late Transition Metal Bulk Metallic Glasses, chapter 1, Bulk Metallic Glasses: An Overview, ed. M. Miller, P. Liaw, New York, USA, 2008, 1-26.
12. Prakash, B., Abrasive Wear Behaviour of Fe, Co and Ni Based Metallic Glasses. Wear, 2005, 258, 217–224.
13. Koga, G. Y., Schulz, R., Savoie, S., Nascimento, A. R. C., Drolet, Y., Bolfarini, C., Kiminami, C. S. and Botta, W. J., Microstructure and Wear Behavior of Fe-based Amorphous HVOF Coatings Produced from Commercial Precursors. Surf. Coat. Technol., 2017, 309, 938–944.
14. Inoue, A., Arnberg, L., Oguchi, M., Backmark, U., Bäckström, N. and Masumoto, T., Preparation of FeCrMoC Amorphous Powders and Microstructure and Mechanical Properties of Their Hot-Pressed Products. Mater. Sci. Eng., 1987, 95, 101–114.
15. Anis, M., Rainforth, W. M. and Davies, H. A., Wear Behaviour of Rapidly Solidified Fe68Cr18Mo2B12 Alloys. Wear, 1994, 172, 135–145.
16. Ahmadi, S., Shahverdi, H. R. and Saremi, S. S., Effects of Nb Alloying on Nano-Crystallization Kinetics. J. Mater. Sci. Technol., 2011, 27, 735–740.
17. Zohdi, H., Shahverdi, H. R. and Hadavi, S. M. M., Effect of Nb Addition on Corrosion Behavior of Fe-based Metallic Glasses in Ringer's Solution for Biomedical Applications. Electrochem. commun., 2011, 13, 840–843.
18. Zohdi, H., Bozorg, M., Arabi Jeshvaghani, R., Shahverdi, H. R. and Hadavi, S. M. M., Corrosion Performance and Metal Ion Release of Amorphous and Nanocrystalline Fe-based Alloys Under Simulated Body Fluid Conditions. Mater. Lett., 2013, 94, 193–196.
19. Hasanabadi, M. F., Ghaini, F. M., Ebrahimnia, M. and Shahverdi, H. R., Production of Amorphous and Nanocrystalline Iron Based Coatings by Electro-spark Deposition Process. Surf. Coat. Technol., 2015, 270, 95–101.
20. Petrzhik, M., Molokanov, V. and Levashov, E., On Conditions of Bulk and Surface Glass Formation of Metallic Alloys. J. Alloys Compd., 2017, 707, 68–72.
21. Gitlevich, A.E., Mikhailov, V.V., Parkanskii, N.Ya. and Reutsky, B. M., Physical Bases of Electro-digged Diesing Metal Surfaces, chapter 1, Electrospark Alloying of Metallic Surfaces, Kishinev, Republic of Moldova, 1985, 7-40 (in Russian).
22. Zamulaeva, E. I., Levashov, E. A., Sviridova, T. A., Shvyndina, N. V. and Petrzhik, M. I., Pulsed Electrospark Deposition of MAX Phase Cr2AlC Based Coatings on Titanium Alloy. Surf. Coatings Technol., 2013, 235, 454–460.
23. Newbury, D. E., Mistakes Encountered During Automatic Peak Identification of Minor and Trace Constituents in Electron-Excited Energy Dispersive X-Ray Microanalysis. Scanning, 2009, 31, 1–11.
24. Kato, K. and Adachi, K., Wear Mechanisms, Part 7, Modern Tribology Handbook, ed. B. Bhushan, New York, USA, 2001, 273–300.
25. Köster, U., Surface Crystallization of Metallic Glasses. Mater. Sci. Eng., 1988, 97, 233–239.
26. Hutchings, I. M., The Challenge of Wear, chapter 1, Wear – Materials, Mechanisms and Practice, ed. G. W. Stachowiak, Chichester, England, 2006, 1–8.
27. Ahmadi, S., Shahverdi, H. R. and Saremi, S. S., Nanocrystallization of Alpha-Fe Crystals in Fe52Cr18Mo7B16C4Nb3 Bulk Amorphous Alloy. J. Mater. Sci. Technol., 2011, 27, 497–502.
28. Ahmadi, S., Shahverdi, H. R., Afsari, M. and

Abdollah-zadeh, A., Nano-crystallization of Fe36Cr12Mo10 Phase in Fe55−xCr18Mo7B16C4Nbx (X=0, 3, 4) Amorphous Alloys. J. Non. Cryst. Solids, 2013, 365, 47–52.

29. Saremi, S. S., Investigation of Crystallization and Nanostructured Phase Formation in Fe55Cr18Mo7B16C4 Amorphous Alloy, Thesis, Tarbiat Modares University, 2011.
30. Duarte, M. J., Kostka, A., Crespo, D., Jimenez, J.A., Dippel, A.C., Renner, F.U. and Dehm, G., Kinetics and Crystallization Path of a Fe-based Metallic Glass Alloy. Acta Mater., 2017, 127, 341–350.
31. Padilha, A. F. and Ronald, L. P., Phase Transformation and Microstructure, Chapter 3, Duplex Stainless Steels, eds. I. Alvarez-Armas and S. Degallaix-Moreuil, London, UK, 2009, 115–139.
32. Duarte, M. J., Kostka, A., Jimenez, J.A., Choi, P., Klemm, J.,Crespo, D., Raabe, D. and Renner, F.U., Crystallization, phase evolution and corrosion of Fe-based metallic glasses: An atomic-scale structural and chemical characterization study. Acta Mater., 2014, 71, 20–30.
33. Kate, K., Classification of WearMechanisms/Models, chapter 2, Wear–Materials, Mechanisms and Practice, ed. G. W. Stachowiak, Chichester, England, 2006, 9–20.